PCCP

ROYAL SOCIETY OF CHEMISTRY

PAPER

View Article Online
View Journal | View Issue

Cite this: *Phys. Chem. Chem. Phys.*, 2022, **24**, 16075

Hydration in aqueous NaCl

Christoph J. Sahle, *[a] Emmanuelle de Clermont Gallerande,[a] Johannes Niskanen,[b] Alessandro Longo,[a] Mirko Elbers,[c] Martin A. Schroer,[d] Christian Sternemann[c] and Sandro Jahn[e]

Received 11th January 2022,
Accepted 27th May 2022

DOI: 10.1039/d2cp00162d

rsc.li/pccp

Atomistic details about the hydration of ions in aqueous solutions are still debated due to the disordered and statistical nature of the hydration process. However, many processes from biology, physical chemistry to materials sciences rely on the complex interplay between solute and solvent. Oxygen K-edge X-ray excitation spectra provide a sensitive probe of the local atomic and electronic surrounding of the excited sites. We used *ab initio* molecular dynamics simulations together with extensive spectrum calculations to relate the features found in experimental oxygen K-edge spectra of a concentration series of aqueous NaCl with the induced structural changes upon solvation of the salt and distill the spectral fingerprints of the first hydration shells around the Na^+- and Cl^--ions. By this combined experimental and theoretical approach, we find the strongest spectral changes to indeed result from the first hydration shells of both ions and relate the observed shift of spectral weight from the post- to the main-edge to the origin of the post-edge as a shape resonance.

1 Introduction

More than a century after the first description of what is now commonly referred to as the Hofmeister series,[1] detailed characterization of the structure and spatial extent of ions' hydration shells is still missing.[2,3] Even though the study of the influence of Hofmeister salts on the stability of proteins has shifted focus from water mediated influences to more direct ion–protein interactions,[4] the understanding of ion–solvent interactions remains of high interest across many fields of research including bio-, biochemical-, chemical-, and technical processes.[2,3,5,6] Already small amounts of solvated NaCl, one of the simplest salts and ubiquitous in everyday life, in water, for example, result in considerable changes in water's macroscopic properties such as viscosity, freezing and boiling points, as well as surface tension.[7]

While the alteration of the water structure in the first hydration shell of the solvated ions is well established, the spatial extent of the cation and anion influence on the water network is still controversially discussed.[8] In an early report on femtosecond optical pump-probe spectroscopy Omta *et al.*[9] described water molecules outside of the first hydration shell of the studied ions to be practically unaffected by the presence of the ions. Later femtosecond time-resolved infrared spectroscopy[10] and terahertz dielectric relaxation spectroscopy[11] on aqueous solutions of different salts revealed that the effect ions have on the structure of water strongly depends on the ions under study and may, in certain cases, be non-additive and observable beyond the first solvation shell.[10] An influence of ions on the oxygen–oxygen radial distribution function (RDF) exceeding first shell distances was also reported based on data from scattering experiments that were analysed using empirical potential structure refinement.[12] The authors relate the observed changes in the O–O RDF to those observed when pure water is subjected to increased pressure, where the perturbation is due to shrinkage of the second and third coordination shells similar to what has been proposed earlier based on neutron scattering.[13,14] The used empirical potential structural refinement method, however, was shown to not necessarily lead to a unique atomic structural solution and requires additional constraints using complementary methods such as X-ray spectroscopy.[15]

X-Ray spectroscopic work using X-ray absorption spectroscopy (XAS) and X-ray Raman scattering (XRS) suggests a small extent of the perturbations of monovalent ions on the water structure.[16,17] A marked difference in the influence of Na^+ on the one hand and Mg^{2+} and Al^{3+} on the other hand on the hydrogen bond network was reported based on a combination

[a] *ESRF, The European Synchrotron, 71 Avenue des Martyrs, CS40220, FR-38043 Grenoble Cedex 9, France. E-mail: christoph.sahle@esrf.fr*
[b] *Department of Physics and Astronomy, University of Turku, FI-20014 Turun Yliopisto, Finland*
[c] *Fakultät Physik/DELTA, Technische Universität Dortmund, D-44221 Dortmund, Germany*
[d] *Nanoparticle Process Technology, University of Duisburg-Essen, D-47057 Duisburg, Germany*
[e] *Institute of Geology and Mineralogy, University of Cologne, D-50674 Köln, Germany*

of XRS and small angle X-ray scattering data.[18] In the same study, Waluyo *et al.*, however, claimed insignificant contributions of the anions to the changes of the water structure upon solvation. In succeeding work, the same authors assigned observed spectral changes at the oxygen K-edge of different aqueous solutions of monovalent salts to changes in the balance of the population of locally distorted and/or strongly hydrogen bonded water species induced mainly by the cations,[19] leaving the question of the anions' role unanswered.

Structural simulations from first principles largely agree with the notion of a relatively small and local influence of solvated ions (both cations and anions) on their immediate surrounding,[20,21] while simulations based on classical force fields have shown both long- and short-range effects, depending on the force-fields used.[22–24] It is often stressed that treating the electronic degrees of freedom explicitly is crucial to reproduce the micro- and macroscopic properties of the aqueous salt solutions.[25,26] Most recent work shows further improvement between experimental observables and simulations when quantum nuclear effects are explicitly taken into account.[27,28]

Here, we address effects of NaCl upon solvation in liquid water by experimental oxygen K-edge spectroscopy using XRS spectroscopy in combination with spectrum calculations for local structures from *ab initio* molecular dynamics (AIMD) simulations. The observed experimental and computed spectral effects are rather weak, which necessitates the advantageous properties of the hard X-ray technique: stability and control of the thermodynamic conditions, bulk sensitivity, and good statistical accuracy. In this work we study the local water structure around a single NaCl ion pair, Na^+, and Cl^- dissociated in an AIMD box. This allows exploring effects of individual ions, otherwise artificially limited by the small size of the typical simulation cells. Our computed ensemble-averaged spectra reproduce the overall trends observed in the experiment well, which motivates closer analysis of individual structures from these simulations. The analysis of the large data set reveals that the oxygen K-edge spectra are mostly affected for water molecules in the direct vicinity of both the cation and anion.

2 Materials and methods

2.1 Experimental spectra

XRS spectroscopy is a special case of non-resonant inelastic X-ray scattering when shallow core-level excitations are involved and, especially at low values of momentum transfer q, yields information comparable to soft X-ray absorption spectroscopy.[45–47] The non-resonant nature of the XRS process, however, renders the measured spectra practically free of saturation and self- or over-absorption artifacts and the use of hard X-rays furthermore offers advantages for the measurement of liquids under well defined temperature and pressure conditions and grants access to samples contained in complex sample environments.[48,49]

All spectra were measured with the large solid angle spectrometer at ID20 of the ESRF[50] using Milli-Q water ($R > 18$ MΩ) for the pure water spectrum and stoichiometric mixtures of Milli-Q water with NaCl (purchased from Acros Organics; 99.5% purity) for spectra of 1, 2, 3, 4, and 5 M aqueous NaCl solution. All solutions were measured after degassing and at a temperature of 21 °C using a miniature liquid flow cell to reduce any effect of X-ray beam induced radiation damage.[51] The photon beam from 3 consecutive U26 undulators was monochromatized with a combination of a Si(111) high-heat-load monochromator and a Si(311) channel-cut post-monochromator. To measure spectra of the O K-edge, we scanned the incident energy between 10.22 and 10.30 keV at a fixed analyzer energy of 9.7 keV (near the backscattering energy of the Si(660) analyzer reflection). We used a beam size of 250 × 250 μm^2 and the overall energy resolution was 0.7 eV. All data was extracted and treated using the XRStools program package.[47] At each concentration, the named energy loss region was scanned multiple times and signals from 36 spherically bent analyzer crystals were measured, checked for consistency, and averaged. The spectra were corrected for the valence electrons' response as described in ref. 47 and 52 and were finally normalized to the f-density in the energy loss interval 580–600 eV as described in ref. 53.

2.2 *Ab initio* molecular dynamics

All AIMD simulations were conducted using the QUICKSTEP module of the CP2K code.[29] Kohn–Sham density functional theory (DFT) using a mixed Gaussian and plane wave approach was used for the electronic structure calculations.[30] For real-space integration we used a multi-grid with 5 levels, a plane-wave cutoff of 800 Ry for the finest level, and a relative cutoff for Gaussian mapping of 70 Ry. The exchange–correlation functional was treated by the PBE functional[31] taking London dispersion interactions into account *via* Grimme's D3 method.[32,33] Pseudopotentials as suggested by Krack *et al.*[34] were used, *i.e.* the oxygen and sodium 1s- as well as the chlorine 1s-, 2s-, and 2p-electrons were included in the pseudocores of Goedecker–Teter–Hutter pseudopotentials.[35] MOLOPT split valence double-zeta valence plus polarization basis sets were used.[36] The used pseudopotentials and basis sets are summarized in Tables 2 and 3 (see Further information).

We performed AIMD simulations for four separate simulation cells: (a) 100 H_2O molecules in a cubic box (box length 14.4049 Å, resulting density 1.001 g cm^{-3}), (b) one Cl^--ion in a cubic box together with 100 H_2O molecules (box length 14.4049 Å, density 1.021 g cm^{-3}), (c) one Na^+-ion in a cubic box of 100 H_2O molecules (box length 14.4049 Å, density 1.014 g cm^{-3}), and (d) one cubic simulation box containing both ions (one Na^+- and one Cl^--ion) and 100 H_2O molecules (box length 14.4049 Å, density 1.034 g cm^{-3}, concentration approximately 0.5 M). All simulation boxes were first equilibrated for 8 and run for 10 picoseconds at 800 K and subsequently quenched to 300 K and run at this temperature for 10 picoseconds. Final production runs were performed for 10 picoseconds at 300 K. For all AIMD runs, the temperature of the canonical ensemble (constant *NVT*) was controlled by

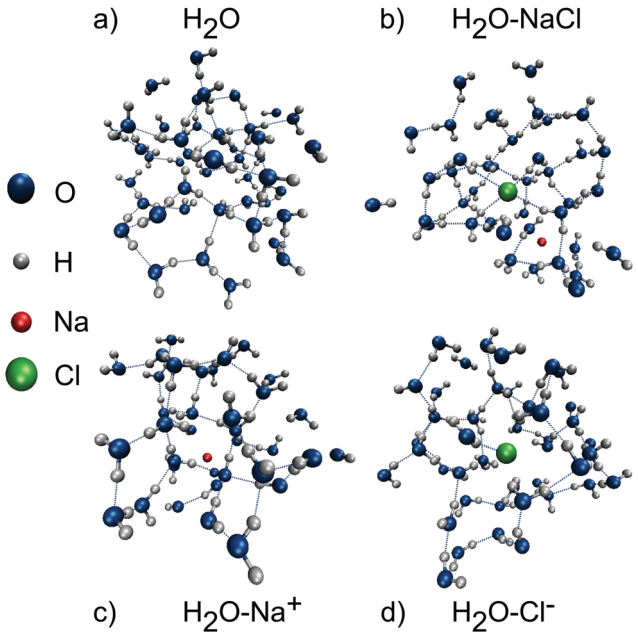

Fig. 1 Ball and stick representations of snapshots from the AIMD simulation trajectories for (a) pure H_2O, (b) H_2O–NaCl, (c) H_2O–Na^+ and (d) H_2O–Cl^-. Oxygen atoms are represented by blue, hydrogen by grey, sodium by red, and chlorine atoms by green spheres. Hydrogen bonds are indicated as thin dashed blue lines.

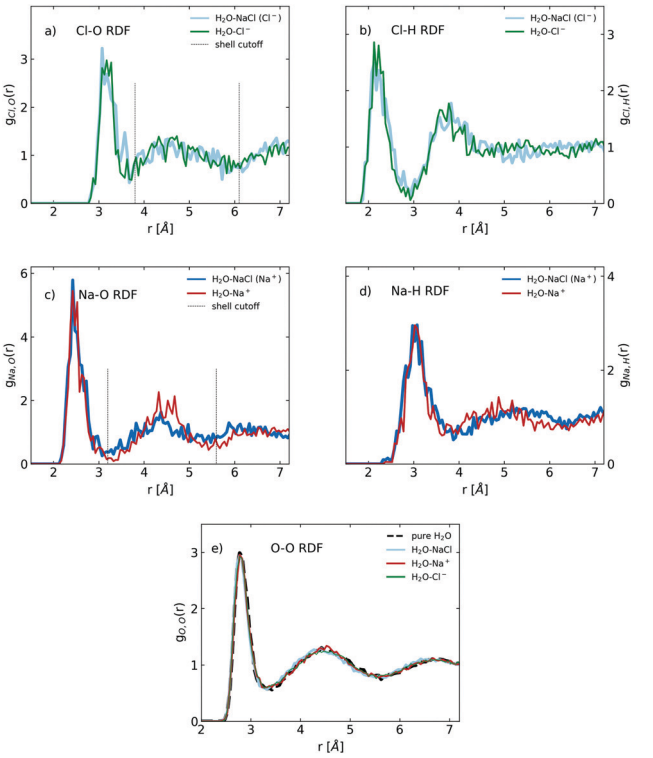

Fig. 2 (a) Cl–O RDFs from the H_2O–NaCl and H_2O–Cl^- snapshots, the cutoff radii for the different hydration shells are indicated by dashed lines. (b) Cl–H RDFs from the H_2O–NaCl and H_2O–Cl^- snapshots. (c) Na–O RDFs from the H_2O–NaCl and H_2O–Na^+ snapshots, the cutoff radii for the different hydration shells are indicated by dashed lines. (d) Na–H RDFs from the H_2O–NaCl and H_2O–Na^+ snapshots. (e) O–O RDF from the simulation snapshots of pure H_2O, H_2O–NaCl, H_2O–Na^+, and H_2O–Cl^-.

canonical sampling through velocity rescaling, CSVR,[37] using a time constant of 1 ps. The equations of state were integrated with a time step of 0.5 fs, and periodic boundary conditions were used. From each of the production run trajectories we extracted 100 equally spaced snapshots for the calculation of theoretical XRS spectra and further analysis (*vide infra*). Examples of the used snapshots are shown as ball and stick representations in Fig. 1(a–d) for pure H_2O, NaCl in water, one Na^+-ion in water, and one Cl^--ion in water, respectively.

RDFs from the snapshots used for the subsequent spectrum calculations and structural analyses are shown in Fig. 2. Parts (a and b) show the partial Cl^-–O and Cl^-–H RDFs for the simulation boxes containing Cl^-–ions, parts (c and d) show the Na^+–O and Na^+–H RDF, and part (e) the O–O partial RDF. These partial RDFs are in almost quantitative agreement with previously published partial RDFs.[21,26]

2.3 Spectrum calculations

Calculations of the XRS spectra of the oxygen K-edge were performed using the Bethe–Salpeter equation (BSE) method as implemented in the OCEAN (Obtaining Core level Excitations using *ab initio* methods and the NIST BSE solver) code.[38–40] For the calculations, the ground state wave functions and electron densities were computed using density functional theory (DFT) with the Quantum ESPRESSO program package.[41,42] The ground state DFT calculations were performed within the local density approximation (LDA) using norm conserving pseudopotentials from the ABINIT repository. A planewave energy cutoff of 70 Ry and $2 \times 2 \times 2$ *k*-point mesh for the ground state electron density proved to be sufficient. The wave functions for the screening and BSE calculation were generated from a non-self-consistent-field calculation using a $2 \times 2 \times 2$ *k*-point mesh. Since we use pseudopotentials for the computation of the ground state electronic properties, projector augmented wave (PAW) reconstructed all-electron wave functions were generated for the calculation of core to valence transition matrix elements.[43] The use of pseudopotentials also results in spectra on energy scales relative to the Fermi level of the respective simulation box and thus the spectra from separate AIMD snapshots are not necessarily on the same absolute energy scale. We therefore shifted all spectra by a rigid energy offset of 535 eV such that the oxygen K-edge pre-peak of bulk water is at 535.5 eV as was found in this and previous experiments. The dielectric screening response was evaluated within a sphere centered around every scattering atom using the random phase approximation and by using the Levine–Louie model dielectric function outside these spheres.[44] Convergence of the final spectra with respect to the sphere radius was confirmed. The solution of the BSE yields the final electron–hole scattering states.

We calculated K-edge spectra for all oxygen atoms from 25 individual simulation snapshots of the neat water AIMD run as

well as 50 snapshots of each of the ion containing simulations resulting in a total of 17 500 individual oxygen K-edge spectra. For all spectrum calculations, the same periodic boundary conditions as employed during the AIMD runs were used.

2.4 Structure characterization

We define a selection of parameters to describe the atomic structure of the liquids in the immediate vicinity of the scattering oxygen atoms as follows. The use of such geometric criteria is motivated by straightforward evaluation of the parameters and by their direct link to structures from the AIMD runs.

2.4.1 Hydrogen bonds. We define hydrogen bonds subject to geometric criteria as defined in ref. 54, 55 and used in ref. 53, 56 and 57 that two H_2O molecules are hydrogen bonded if the oxygen–oxygen separation is less than 3.5 Å and the hydrogen-donor–acceptor angle is less than or equal to 30°. Following the ideas of Mancinelli *et al.* ref. 58 of strong Cl^-–water interactions, in addition to hydrogen bonding between two water molecules, we consider water molecules as hydrogen-donor bonded with a Cl^--ion using the same geometric criteria as for the oxygen acceptor. Other approaches to characterize hydrogen-bonding exist, however, they have been shown to lead to comparable results.[59]

2.4.2 Ion hydration and solvation shells. We consider the hydration of the solvated ions based purely on distance criteria and use the minima of the partial Cl^-–O and Na^+–O RDFs as cutoff distances to define solvation shells around the respective ions. These RDFs are presented in Fig. 2(a and c) and their minima are identified at approximately 3.8, 6.1, and 7.9 Å for the Cl^-–O RDF and at approximately 3.2, 5.6, and 7.5 Å for the Na^+–O RDF, respectively. Due to the finite simulation box size, the fourth hydration shell is not completely covered by the simulations. Variations of these cutoffs were tested and essentially led to the same conclusions. A summary of the average number of H_2O molecules in the different hydration shells is provided in Table 1.

3 Results

A direct comparison of the experimental oxygen K-edge data and the simulation averages is shown in Fig. 3(a and b). Difference spectra with respect to the spectrum of pure H_2O are shown in part (c and d) for the experimental and computational results, respectively. The three main features of the oxygen K-edge, pre (I), main (II), and post-edge (III), are shaded in grey. Error-bars, shown for every fifth data point of the experimental spectra and differences, are almost of the order of the line-width and will therefore be omitted hereafter.

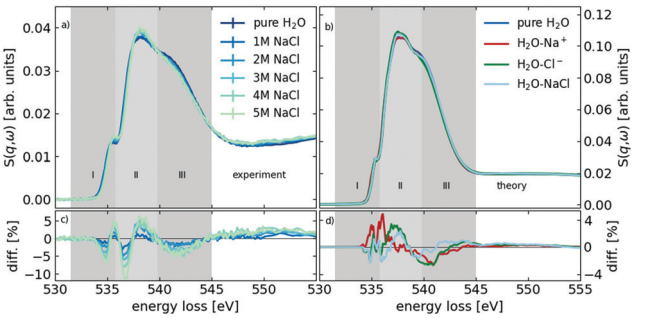

Fig. 3 (a) Experimental O K-edge XRS spectra of differently concentrated aqueous NaCl solutions. (b) Averages over all oxygen K-edge spectra from all snapshots of the respective AIMD simulation trajectories. (c) Experimental difference spectra with respect to the spectrum of pure H_2O. (d) Difference spectra of the calculations using the ion containing simulation boxes with respect to those of the simulation box of pure H_2O.

It is evident that the computed spectra are compressed along the energy loss axis compared to the experimental spectra, which we attribute mainly to the inherent errors of DFT to accurately predict the electronic structure and describe electronic excited states in the materials.[60]

The experimental spectra of the different aqueous NaCl solutions show systematic changes with increasing concentration. The pre-edge (I) shifts slightly to higher energy loss values and its intensity increases with increasing NaCl concentration. Concomitantly, spectral weight is shifted from the post-edge (III) to the main-edge (II) with increasing salt concentration.

All simulation averages show relatively minor changes in the pre-edge intensity with a slightly increased pre-edge intensity if a Cl^--ion is present. A clear shift of spectral weight from the post- to the main-edge is observable between the simulation results of pure H_2O and the aqueous NaCl solution, as observed for the experimental spectra of the concentration series.

When comparing the difference spectra in part (c and d) of the figure, it is evident that difference spectra obtained using the calculations based on the Cl^--ion containing simulations show the characteristic features observed in the experimental difference curves, while the difference spectrum obtained using the calculation based on the simulation box containing only one Na^+-ion is markedly different.

We examine the hydration of the Na^+- and Cl^--ions by comparing spectra of water molecules from the different hydration shells as defined above. These spectra are shown in Fig. 4(a) for the Cl^--ion and part (b) for the hydration of the Na^+-ion together with the spectrum of pure H_2O (black line). Difference spectra with respect to that of pure H_2O are shown in part (c and d) of the same figure. All spectra are normalized by the respective area in the range 532 to 555 eV and are not weighted by the population of the respective hydration shells. We therefore examine the differences in spectral shape from

Table 1 Number of H_2O molecules in the different hydration shells around the Cl^-- and Na^+-ions. All numbers represent mean values over all used structural snapshots. The errors represent standard deviations from the mean. Note that due to the finite simulation box sizes, the fourth shell is not completely covered by the simulations

H_2O mol. per ion	Na^+	Cl^-
Total	100.00 ± 0.00	100.00 ± 0.00
Shell 1	5.20 ± 0.06	6.24 ± 0.15
Shell 2	19.35 ± 0.21	24.22 ± 0.31
Shell 3	32.87 ± 0.36	35.14 ± 0.49
Shell 4	42.58 ± 0.28	34.41 ± 0.36

one hydration shell to another rather than the absolute contribution of each shell to the overall difference observed in the total averages of spectra shown in Fig. 3.

The pre-edge of the spectra of the different shells around the Cl^--ion varies little. The most drastic changes are found at the main- and post-edge of the spectrum of the first shell with a largely enhanced main- and grossly reduced post-edge. Hydration shells 2, 3, and 4 exhibit only small variations compared to the spectrum of pure H_2O. For the hydration shells around the Na^+-ions we find considerably increased spectral weight in the pre-edge region for the spectrum of the first hydration shell as well as an enhanced main- and depleted post-edge. The latter, however, to smaller degree than found for the Cl^--ions. The shape of the spectrum from the higher hydration shells closely resemble that of pure H_2O with only minor differences, as was the case for the Cl^--ion containing simulation box (compare Fig. 4(d)).

In order to analyze the structural changes in the water network induced by solvation of the Na^+- and Cl^--ions, we extracted the total number of hydrogen bonds and the average hydrogen bond angle per water molecule for all H_2O molecules from the different hydration shells. The results are shown in Fig. 5.

If hydrogen-donor bonding with Cl^- is accounted for, the number of hydrogen bonds (Fig. 5(a)) around the Cl^--ions (green solid) is close to that found in pure H_2O (solid black line). If hydrogen bonding between water and the Cl^--ion is not accounted for (green dashed line), the number of hydrogen bonds found in the first hydration shell is correspondingly lower.

Around the Na^+-ions (solid red line), the number of hydrogen bonds is depleted in the first hydration shell, slightly increased in the second shell and approaches that of pure H_2O for the third and fourth shell. The difference between the number of hydrogen bonds in pure H_2O (solid black line) and aqueous NaCl solutions (dashed-dotted black line) is therefore solely to be attributed to the inability of the water molecule to donate hydrogen bonds to Na^+. The results are in almost

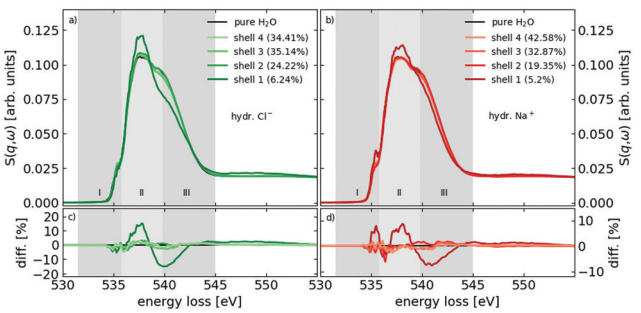

Fig. 4 Average spectra for the different hydration shells around the Cl^--ions (part a) and Na^+-ions (part b) in comparison with the spectrum of pure H_2O (black solid line) and the difference spectra with respect to that of pure H_2O (parts (c and d), note different ordinate scales). Numeric distributions of water molecules within the simulation cells to ion-centered solvation shells are provided in the legend.

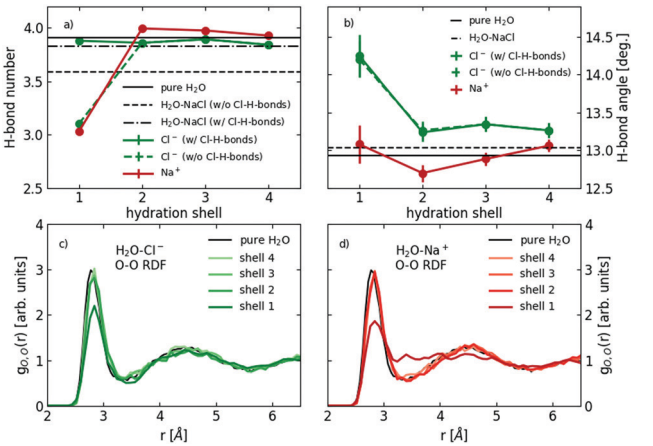

Fig. 5 (a) Total number of hydrogen bonds per water molecule for the different hydration shells around the Na^+- and Cl^--ions in comparison with the average number of hydrogen bonds found in pure H_2O (black line) and aqueous NaCl (dashed and dashed-dotted lines). (b) Mean hydrogen bond angle for the water molecules in the different hydration shells around the Na^+ and Cl^- ions. (c) $O–O_{(i=1,2,3,4)}$ RDFs for the Cl^--ion containing AIMD snapshots. (d) Same as (c) but for the Na^+-ion containing AIMD simulation snapshots.

quantitative agreement with earlier studies when hydrogen bonding with Cl^- is omitted.[21]

The hydrogen bond angles in the direct vicinity of the Cl^--ions are considerably distorted (red, Fig. 5(b)), but rapidly approach those found in pure H_2O. The hydrogen bond angles around the Na^+-ion (red) are less disturbed in the first shell, but are slightly more directed in the second and third shell before likewise approaching the values found in pure H_2O (solid black line) and aqueous NaCl (dashed black line).

The $O–O_{(i=1,2,3,4)}$ RDFs for the different shells around the Cl^--ion are shown in part (c) and for the different shells around the Na^+-ion in part (d) of Fig. 5, respectively. For both ions, the RDF of the first hydration shell shows a reduced peak intensity at approximately r = 2.8 Å, *i.e.* the nearest neighbor correlation distance. This loss, the excluded volume effect, is due to the presence of the ions. Around the Cl^--ion, changes besides the apparent reduction of the first peak are small and RDFs of hydration shells 2, 3, and 4 almost coincide with the reference O–O RDF from pure H_2O. The RDF of the first shell around the Na^+-ion (part d), however, is markedly washed out with a lack of a clear minimum between the first and the second hydration shell (between r = 3–4 Å), and a considerably reduced height at r = 4.5 Å in comparison with the RDF of pure H_2O. The RDFs of the higher hydration shells again coincide with that of pure H_2O within the statistical accuracy.

4 Discussion

The oxygen K-edge spectrum has proven to be a powerful probe of the local atomic and electronic structure around an absorbing or scattering oxygen site in water and aqueous solutions.[17,53,56,57,61–69] The pre-edge feature of the oxygen edge found at an excitation energy of 535.5 eV is enhanced if the

water–water hydrogen bond network is highly distorted and/or broken. This is the case, for example, at elevated temperatures and at supercritical conditions.[61,62] The main-edge feature, centered around 539 eV, has been associated with localized excitations,[70] and thus increases with increasing density, as for example in high pressure ice phases when the second shell water molecules penetrate into the first shell.[70,71] The main-edge was also observed to increase with increasing disorder.[61,62] Finally, the post-edge at around 541 eV is prominent in a well ordered and strongly hydrogen bonded environment, for example found in the low pressure crystalline ice phases.[53,70,71]

It is instructional to compare the structures of ice Ih, ice Ic, and ice III, all of which have H_2O molecules coordinated by four other H_2O molecules, two *via* donor hydrogen bonds and two *via* acceptor hydrogen bonds, with structures of the high pressure ice phases ice VI and ice VII, both of which are made up of two interpenetrating sub-lattices and therefore have four nearest oxygen neighbors coordinated *via* hydrogen bonds and four nearest oxygen neighbors that are not hydrogen bonded. Whereas the oxygen K-edge spectra of the low-pressure ice phases are characterized by a prominent post-edge, the spectra of the high-pressure ices phases are dominated by the main-edge feature.[70–72] Niskanen *et al.* pointed out that the post-edge region is found at energy losses greater than the binding energy of the oxygen 1s electron ($E_{\mathrm{bind,1s}}$ = 538.21 eV)[73] and constitutes a continuum or shape resonance.[53,74] The energy loss position of the post-edge is compatible with nodes of the photo-electronic wave function at approximately 3.1 and 4.6 Å, *i.e.* of the order of the first and second coordination shells in the low-pressure ice phases. Introduction of additional nearest neighbors due to a second non-hydrogen bonded sublattice, as for the high-pressure ice phases, or the loss of local order, as for liquid and supercritical water, destroy the potential barriers and, therefore, prevent the formation of such shape resonances. It was recently shown that the phenomenological relationships between the microscopic structure of water and the different features of the oxygen excitation spectrum (pre-edge, main-edge, and post-edge) can be put on a statistical footing and these observations for the liquid state must be viewed as structural fingerprints of a statistical ensemble.[53,56]

Following the mentioned phenomenological reasoning, the transfer of spectral weight from the post-edge to the main-edge concomitant with a slight increase of the pre-edge upon solvation of NaCl infers increasing distortions and disorder of the hydrogen bond network as well as increased oxygen–oxygen coordination as observed in the high pressure ice phases. The latter, however, seem contradictory to the fact that the overall density increase with increasing salt content is small.[75]

The most prominent spectral change in the concentration series is the transfer of spectral weight from the post-edge to the main edge in accord with earlier XAS and XRS measurements of the oxygen K-edge of aqueous NaCl solutions.[16,18,68,69,76,77] As elaborated above, the post-edge feature constitutes a shape resonance due to the potential barrier formed by the nearest and next-nearest oxygen neighbors.[53,74] It is therefore natural to seek the explanation of the spectral changes observed in the experimental concentration series as well as the solvation-shell-dependent variation in post-edge intensity in the conditions for a shape resonance.

According to the O–O RDFs calculated from the perspective of oxygen atoms assigned to the different ion solvation shells as shown in Fig. 5(c and d), we observe a substantially reduced height of the first O–O correlation peak of oxygens in the first coordination shell around both the Cl^-- and Na^+-ions. Interestingly, this reduction is observed even for oxygens in the second ion solvation shell in the case of the Na^+-ion. This implies that around oxygen atoms in the direct vicinity of the ions, heavily distorted potential barriers exist for the continuum scattering resonance to originate from; the position relative to the oxygen neighbors and electronic structure as well as the relative position of the ions are markedly different compared to the oxygen–oxygen coordinations found in pure H_2O leading to these distorted potential barriers. This observation readily explains the loss of intensity in the post-edge region observed for the first ionic solvation shell (Fig. 4) and is in accord with experimental and theoretical findings that observe perturbations of the water structure.[3] The Na^+-ion coordinates water molecules with the oxygen atom pointing toward the ion and hydrogen atoms pointing away from the ion,[58,78,79] locally altering the balance between water hydrogen bond donors and acceptors also in the second shell.[80] The Cl^--ion can accept hydrogen bonds and (path-integral) *ab initio* simulations show that the polarizability of the Cl^--ion leads to an asymmetric coordination of water molecules around them.[26,81]

As mentioned by Näslund *et al.*[16] relatively large amounts of solvated NaCl are needed for appreciable spectral changes in the oxygen K-edge, pointing, by way of stoichiometric consideration, to a localized and short ranged change of the water network around the ions. A similar trend was found for highly soluble LiCl.[17] Following the approach of Juurinen *et al.*, we plot the intensity ratios of the main- and post-edge spectral features as a function of NaCl concentration in Fig. 6(a). Error-bars are estimated by varying the integration ranges for the two spectral features by $\Delta E = \pm 0.2$ eV, and linear fits (dashed lines) serve as guides to the eye. A linear dependence of the main-to-post-edge ratio is evident up to concentrations of 3 M NaCl. Scaled to the typical box sizes and densities used here, we would find between 5 and 6 ion pairs in a volume of 80–85 water molecules at a NaCl concentration of 3 M. Taking into account the number of water molecules found in the first hydration shell of Na^+ and Cl^- (compare Table 1), at 3 M almost all water molecules would be found in the first shell of one of the ions. Interestingly, spectral saturation was not observed in an earlier X-ray absorption spectroscopy experiment in transmission geometry even at concentrations close to the solubility limit.[19]

Assuming a linear dependence of the spectral changes upon increasing NaCl concentration, we used the spectra of pure H_2O, 1 M, 2 M, and 3 M NaCl in a non-negative matrix factorization scheme as was previously presented for aqueous solutions of TMAO and urea,[57,65] and extracted a

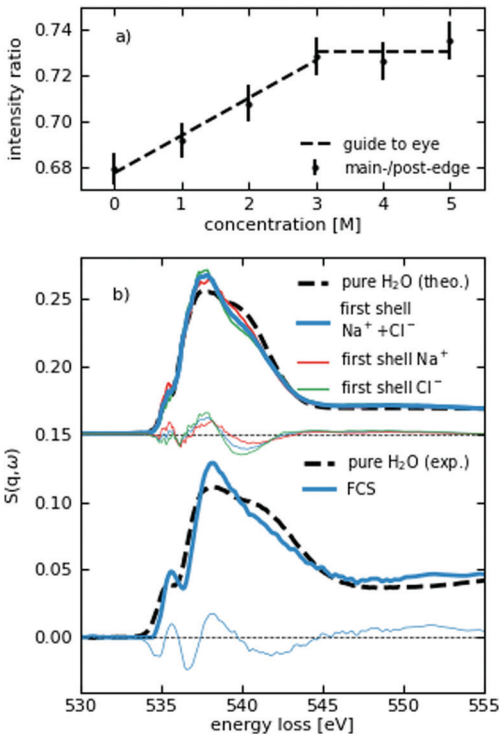

Fig. 6 (a) Main-to-post-edge ratio of the experimental O K-edge data *versus* NaCl concentration. (b) Non-negative matrix factorization analysis of the experimental spectra from the concentration series in comparison to calculated spectra from oxygen atoms of the first hydration shell around the Na^+- and Cl^--ions.

free-component-spectrum (FCS) by constraining the spectrum of pure H_2O as a reference and forcing the component weights to change linearly with increasing NaCl concentration (increasing component weight for the FCS with increasing NaCl concentration and decreasing component weight for the pure H_2O spectrum). The result of this procedure is shown in Fig. 6(b) (bottom) in direct comparison to a weighted average spectrum of the oxygen atoms of the first hydration shell around the Na^+- and Cl^--ion (top). Difference spectra with respect to those of pure H_2O (black dashed lines) are also shown as thin green lines. As for the case of the hydration of the osmolytes TMAO and urea, the resemblance of the FCS and the calculated spectrum of the first hydration shell is remarkable except for a more intense and separated pre-edge feature found in the FCS compared to the simulation results. This striking similarity of the experimental FCS and a superposition of simulated spectra from the immediate surrounding of the ions suggests that the first solvation shell around the two ions dominates the overall spectrum and therefore the effect of ion solvation in H_2O must be a rather local effect acting mainly on the first hydration shell.

The spectral changes observed with increasing salt concentration are similar to the differences observed between the low- and high-pressure ice phases as discussed above: increase in main-edge intensity and decrease in post-edge intensity.[70,71] The FCS resembles the O K-edge spectra of pure H_2O measured at supercritical conditions.[61] In terms of local atomic structure, the similarities between the effect of increased pressure and/or disorder on the one hand and the addition of ions on the other hand on the shape of the spectrum in the post-edge region can be reconciled within the framework of the post-edge as a shape resonance. In the case of the high pressure ice phases, it is the collapse of the second nearest neighbors into the first shell that destroys the potential barrier necessary for a shape resonance to occur, in the case of supercritical water it is the strong increase in disorder, and in the case of NaCl, it is the presence of Na^+- and Cl^--ions in the direct proximity of the water molecules that prevent the formation of a potential barrier.

The comparison between the FCS and the spectra of the first ion solvation shells from simulation, however, shows differences in the pre-edge intensity with a more pronounced pre-edge in the experimentally extracted spectrum compared to the simulation result. As mentioned earlier, the pre-edge has been connected to hydrogen bonding and its intensity is increased especially in systems containing water molecules with distorted and broken hydrogen bonds. Recent advancements of structural simulations show that the inclusion of nuclear quantum effects softens hydrogen bonding in pure water and therefore leads to more realistic pre-edge features.[27,82] More importantly, DelloStritto[26] showed that the choice of DFT exchange and correlation functional influences the Cl–H and Cl–O RDFs and PBE + D3, as used in the current work, results in slightly overstructured Cl–O and Cl–H RDFs indicative of overstructured Cl^--hydration and longer H-bond lifetimes. Furthermore, explicit account of quantum nuclear effects changes the solvation of the Cl^--ion by decreasing the hydrogen bond strength between Cl^- and water even more than that between water and water.[28,81] In the present work nuclear quantum effects are not taken into account, possibly explaining the remaining differences between the FCS and the simulated spectra of the first hydration shells in the vicinity of the pre-edge region. It would be extremely interesting to confront simulated oxygen K-edge spectra based on atomic structures from path-integral molecular dynamics simulations with the experimentally extracted FCS.

5 Conclusions

The systematic spectral changes found in the oxygen K-edge X-ray Raman scattering spectra of aqueous solutions of NaCl with increasing NaCl concentration can be explained to a high degree by extensive statistical simulations based on *ab initio* molecular dynamics and subsequent spectral simulations based on solving the Bethe–Salpeter equation. The most prominent change is the transfer of spectral weight from the post-edge to the main-edge with increasing NaCl concentration. The simulations show that most of the observed difference between oxygen K-edge spectra of the NaCl solution and pure H_2O stem from the modification of the water structure in the first hydration shell around both ions. The dramatic loss of intensity in the post-edge region is readily explained by its nature of a shape

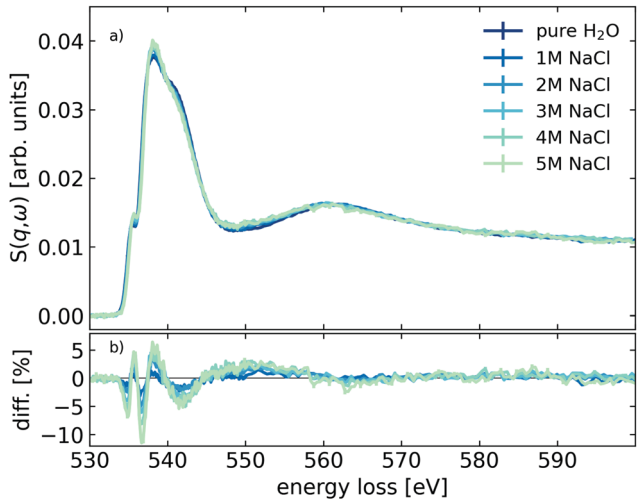

Fig. 7 (a) Oxygen K-edge spectra of pure H_2O and differently concentrated aqueous NaCl solutions. (b) Spectral differences with respect to the pure H_2O spectrum.

resonance: the presence of the Na^+- and Cl^--ions in the first coordination shell heavily distorts the potential barriers necessary for the resonance to exist.

A short range influence of the solvation of NaCl is further corroborated by observation of a saturated oxygen K-edge shape at 3 M NaCl *via* stoichiometric considerations. We use non-negative matrix factorization of the experimental spectra up to 3 M to extract a free component spectrum that closely resembles the simulated oxygen K-edges from the first hydration shells around Na^+ and Cl^-. As was found for the hydration of the organic osmolyte TMAO and urea, the extracted free component spectrum represents the most drastic changes in spectral shape induced by the hydration of the Na^+- and Cl^--ions. Remaining differences between experiment and theory are attributed to the used density functional resulting in slightly overstructured first hydration shells.

The overall shape of the oxygen K-edge spectra of water molecules from the first ion hydration shell around Na^+ and Cl^- resemble the spectra of water at elevated and supercritical conditions as well as of the high pressure ice phases VI and VII. Likewise, the radial distribution function from the first hydration shell around Na^+ ($O–O_{(i=1)}$) shows signatures of predicted radial distribution functions of high-density water.[14,83] However, the reason for these resemblances is the presence of Na^+- and Cl^--ions rather than an approaching second neighbor coordination shell. It would be interesting to directly compare O K-edge spectra from monovalent salt solutions with those of pure H_2O at elevated pressures.

Table 2 Pseudopotentials used for the molecular dynamics simulations

Atom	Pseudopotential[a]
H	GTH-PBE-q1
O	GTH-PBE-q6
Na	GTH-PBE-q9
Cl	GTH-PBE-q7

[a] Naming convention as used in ref. 34.

Table 3 Basis functions used for the molecular dynamics simulations

Atom	Basis set name[a]
H	DZVP-MOLOPT-SR-GTH
O	DZVP-MOLOPT-GTH
Na	DZVP-MOLOPT-SR-GTH
Cl	DZVP-MOLOPT-SR-GTH

[a] Naming convention as used in ref. 36.

6 Further information

Fig. 7 shows the full normalization-range experimental spectra in part (a) and the difference spectra with respect to the pure H_2O spectrum in part (b).

Table 2 contains the pseudopotentials used for the molecular dynamics simulations.

Table 3 contains the used molecularly optimised basis functions as described in ref. 36.

Conflicts of interest

There are no conflicts of interest to declare.

Acknowledgements

The European Synchrotron Radiation Facility is acknowledged for providing synchrotron radiation and computing resources. C. Henriquet and F. Gerbon are kindly acknowledged for the technical support. ME and CS acknowledge funding *via* BMBF project number 05K16PE1 and thank Metin Tolan for supporting these activities. JN acknowledges the Academy of Finland for funding *via* project 331234. Computing time for AIMD simulations was provided by the Gauss Centre for Supercomputing e.V. through the John von Neumann Institute for Computing (NIC) on the JUWELS supercomputer at Jülich Supercomputing Centre (JSC).

Notes and references

1 F. Hofmeister, *Arch. Exp. Pathol. Pharmakol.*, 1888, **24**, 247–260.
2 H. Ohtaki and T. Radnai, *Chem. Rev.*, 1993, **93**, 1157–1204.
3 Y. Marcus, *Chem. Rev.*, 2009, **109**, 1346–1370.
4 P. Jungwirth and P. S. Cremer, *Nat. Chem.*, 2014, **6**, 261–263.
5 B. E. Conway, *Ionic hydration in chemistry and biophysics*, 1981, **https://www.osti.gov/etdeweb/biblio/5193576**.
6 P. Lo Nostro and B. W. Ninham, *Chem. Rev.*, 2012, **112**, 2286–2322.
7 D. R. Lide, *CRC handbook of chemistry and physics*, CRC Press, 2004, vol. 85.
8 D. Paschek and R. Ludwig, *Angew. Chem.*, 2011, **50**, 352–353.

9 A. W. Omta, M. F. Kropman, S. Woutersen and H. J. Bakker, *Science*, 2003, **301**, 347–349.
10 K. Tielrooij, N. Garcia-Araez, M. Bonn and H. Bakker, *Science*, 2010, **328**, 1006–1009.
11 J. T. O'Brien, J. S. Prell, M. F. Bush and E. R. Williams, *J. Am. Chem. Soc.*, 2010, **132**, 8248–8249.
12 R. Mancinelli, A. Botti, F. Bruni, M. Ricci and A. Soper, *Phys. Chem. Chem. Phys.*, 2007, **9**, 2959–2967.
13 R. Leberman and A. Soper, *Nature*, 1995, **378**, 364–366.
14 A. K. Soper and M. A. Ricci, *Phys. Rev. Lett.*, 2000, **84**, 2881.
15 K. T. Wikfeldt, M. Leetmaa, M. P. Ljungberg, A. Nilsson and L. G. Pettersson, *J. Phys. Chem. B*, 2009, **113**, 6246–6255.
16 L.-Å. Näslund, D. C. Edwards, P. Wernet, U. Bergmann, H. Ogasawara, L. G. Pettersson, S. Myneni and A. Nilsson, *J. Phys. Chem. A*, 2005, **109**, 5995–6002.
17 I. Juurinen, T. Pylkkanen, K. O. Ruotsalainen, C. J. Sahle, G. Monaco, K. Hämäläinen, S. Huotari and M. Hakala, *J. Phys. Chem. B*, 2013, **117**, 16506–16511.
18 I. Waluyo, C. Huang, D. Nordlund, U. Bergmann, T. M. Weiss, L. G. Pettersson and A. Nilsson, *J. Chem. Phys.*, 2011, **134**, 064513.
19 I. Waluyo, D. Nordlund, U. Bergmann, D. Schlesinger, L. G. Pettersson and A. Nilsson, *J. Chem. Phys.*, 2014, **140**, 244506.
20 M. Śmiechowski, J. Sun, H. Forbert and D. Marx, *Phys. Chem. Chem. Phys.*, 2015, **17**, 8323–8329.
21 A. P. Gaiduk and G. Galli, *J. Phys. Chem. Lett.*, 2017, **8**, 1496–1502.
22 S. Funkner, G. Niehues, D. A. Schmidt, M. Heyden, G. Schwaab, K. M. Callahan, D. J. Tobias and M. Havenith, *J. Am. Chem. Soc.*, 2012, **134**, 1030–1035.
23 J. Chandrasekhar and W. L. Jorgensen, *J. Chem. Phys.*, 1982, **77**, 5080–5089.
24 S. J. Irudayam and R. H. Henchman, *J. Chem. Phys.*, 2012, **137**, 034508.
25 Y. Ding, A. A. Hassanali and M. Parrinello, *Proc. Natl. Acad. Sci. U. S. A.*, 2014, **111**, 3310–3315.
26 M. DelloStritto, J. Xu, X. Wu and M. L. Klein, *Phys. Chem. Chem. Phys.*, 2020, **22**, 10666–10675.
27 Z. Sun, L. Zheng, M. Chen, M. L. Klein, F. Paesani and X. Wu, *Phys. Rev. Lett.*, 2018, **121**, 137401.
28 F. Tang, J. Xu, D. Y. Qiu and X. Wu, *Phys. Rev. B: Condens. Matter Mater. Phys.*, 2021, **104**, 035117.
29 T. D. Kühne, M. Iannuzzi, M. Del Ben, V. V. Rybkin, P. Seewald, F. Stein, T. Laino, R. Z. Khaliullin, O. Schütt and F. Schiffmann, *et al.*, *J. Chem. Phys.*, 2020, **152**, 194103.
30 J. VandeVondele, M. Krack, F. Mohamed, M. Parrinello, T. Chassaing and J. Hutter, *Comput. Phys. Commun.*, 2005, **167**, 103–128.
31 J. P. Perdew, K. Burke and M. Ernzerhof, *Phys. Rev. Lett.*, 1996, **77**, 3865.
32 S. Grimme, J. Antony, S. Ehrlich and H. Krieg, *J. Chem. Phys.*, 2010, **132**, 154104.
33 R. Jonchiere, A. Seitsonen, G. Ferlat, A. Saitta and R. Vuilleumier, *J. Chem. Phys.*, 2011, **135**, 154503.
34 M. Krack, *Theor. Chem. Acc.*, 2005, **114**, 145–152.
35 S. Goedecker, M. Teter and J. Hutter, *Phys. Rev. B: Condens. Matter Mater. Phys.*, 1996, **54**, 1703.
36 J. VandeVondele and J. Hutter, *J. Chem. Phys.*, 2007, **127**, 114105.
37 G. Bussi, D. Donadio and M. Parrinello, *J. Chem. Phys.*, 2007, **126**, 014101.
38 J. Vinson, J. Rehr, J. Kas and E. Shirley, *Phys. Rev. B: Condens. Matter Mater. Phys.*, 2011, **83**, 115106.
39 J. Vinson, J. Kas, F. Vila, J. Rehr and E. Shirley, *Phys. Rev. B: Condens. Matter Mater. Phys.*, 2012, **85**, 045101.
40 K. Gilmore, J. Vinson, E. Shirley, D. Prendergast, C. Pemmaraju, J. Kas, F. Vila and J. Rehr, *Comput. Phys. Commun.*, 2015, **197**, 109–117.
41 P. Giannozzi, S. Baroni, N. Bonini, M. Calandra, R. Car, C. Cavazzoni, D. Ceresoli, G. Chiarotti, M. Cococcioni and I. Dabo, *et al.*, *J. Phys.: Condens. Matter*, 2009, **21**, 395502.
42 Quantum ESPRESSO, 2019, **http://www.quantum-espresso.org**.
43 G. Kresse and D. Joubert, *Phys. Rev. B: Condens. Matter Mater. Phys.*, 1999, **59**, 1758.
44 Z. H. Levine and S. G. Louie, *Phys. Rev. B: Condens. Matter Mater. Phys.*, 1982, **25**, 6310.
45 Y. Mizuno and Y. Ohmura, *J. Phys. Soc. Jpn.*, 1967, **22**, 445–449.
46 W. Schülke, *Electron dynamics by inelastic X-ray scattering*, Oxford University Press, 2007, vol. 7.
47 C. Sahle, A. Mirone, J. Niskanen, J. Inkinen, M. Krisch and S. Huotari, *J. Synchrotron Radiat.*, 2015, **22**, 400–409.
48 C. Sternemann and M. Wilke, *High Press. Res.*, 2016, **36**, 275–292.
49 C. J. Sahle, A. Rosa, M. Rossi, V. Cerantola, G. Spiekermann, S. Petitgirard, J. Jacobs, S. Huotari, M. Moretti Sala and A. Mirone, *J. Synchrotron Radiat.*, 2017, **24**, 269–275.
50 S. Huotari, C. J. Sahle, C. Henriquet, A. Al-Zein, K. Martel, L. Simonelli, R. Verbeni, H. Gonzalez, M.-C. Lagier and C. Ponchut, *et al.*, *J. Synchrotron Radiat.*, 2017, **24**, 521–530.
51 C. J. Sahle, C. Henriquet, M. A. Schroer, I. Juurinen, J. Niskanen and M. Krisch, *J. Synchrotron Radiat.*, 2015, **22**, 1555–1558.
52 H. Sternemann, C. Sternemann, G. Seidler, T. Fister, A. Sakko and M. Tolan, *J. Synchrotron Radiat.*, 2008, **15**, 162–169.
53 J. Niskanen, M. Fondell, C. Sahle, S. Eckert, R. Jay, K. Gilmore, A. Pietzsch, M. Dantz, X. Lu and D. McNally, *et al.*, *Proc. Natl. Acad. Sci. U. S. A.*, 2019, **116**, 4058–4063.
54 W. Chen, X. Wu and R. Car, *Phys. Rev. Lett.*, 2010, **105**, 017802.
55 A. Luzar and D. Chandler, *Phys. Rev. Lett.*, 1996, **76**, 928.
56 J. Niskanen, C. Sahle, K. Gilmore, F. Uhlig, J. Smiatek and A. Föhlisch, *Phys. Rev. E*, 2017, **96**, 013319.
57 C. J. Sahle, M. A. Schroer, J. Niskanen, M. Elbers, C. M. Jeffries and C. Sternemann, *Phys. Chem. Chem. Phys.*, 2020, **22**, 11614–11624.
58 R. Mancinelli, A. Botti, F. Bruni, M. Ricci and A. Soper, *J. Phys. Chem. B*, 2007, **111**, 13570–13577.
59 S. Chowdhuri and A. Chandra, *Phys. Rev. E: Stat., Nonlinear, Soft Matter Phys.*, 2002, **66**, 041203.
60 K. Burke, *J. Chem. Phys.*, 2012, **136**, 150901.

61 C. J. Sahle, C. Sternemann, C. Schmidt, S. Lehtola, S. Jahn, L. Simonelli, S. Huotari, M. Hakala, T. Pylkkänen and A. Nyrow, *et al.*, *Proc. Natl. Acad. Sci. U. S. A.*, 2013, **110**, 6301–6306.
62 T. Pylkkanen, A. Sakko, M. Hakala, K. Hämäläinen, G. Monaco and S. Huotari, *J. Phys. Chem. B*, 2011, **115**, 14544–14550.
63 I. Juurinen, T. Pylkkanen, C. J. Sahle, L. Simonelli, K. Hämäläinen, S. Huotari and M. Hakala, *J. Phys. Chem. B*, 2014, **118**, 8750–8755.
64 J. Niskanen, C. J. Sahle, I. Juurinen, J. Koskelo, S. Lehtola, R. Verbeni, H. Müller, M. Hakala and S. Huotari, *J. Phys. Chem. B*, 2015, **119**, 11732–11739.
65 C. Sahle, M. Schroer, I. Juurinen and J. Niskanen, *Phys. Chem. Chem. Phys.*, 2016, **18**, 16518–16526.
66 C. Sahle, J. Niskanen, C. Schmidt, J. Stefanski, K. Gilmore, Y. Forov, S. Jahn, M. Wilke and C. Sternemann, *J. Phys. Chem. B*, 2017, **121**, 11383–11389.
67 C. J. Sahle, J. Niskanen, K. Gilmore and S. Jahn, *J. Electron Spectrosc. Relat. Phenom.*, 2018, **222**, 57–62.
68 C. Sahle, M. Schroer, C. Jeffries and J. Niskanen, *Phys. Chem. Chem. Phys.*, 2018, **20**, 27917–27923.
69 M. Elbers, C. Schmidt, C. Sternemann, C. J. Sahle, S. Jahn, C. Albers, R. Sakrowski, H. Gretarsson, M. Sundermann and M. Tolan, *et al.*, *Phys. Chem. Chem. Phys.*, 2021, **23**, 14845–14856.
70 S. T. John, D. M. Shaw, D. D. Klug, S. Patchkovskii, G. Vankó, G. Monaco and M. Krisch, *Phys. Rev. Lett.*, 2008, **100**, 095502.
71 T. Pylkkänen, V. M. Giordano, J.-C. Chervin, A. Sakko, M. Hakala, J. A. Soininen, K. Hämäläinen, G. Monaco and S. Huotari, *J. Phys. Chem. B*, 2010, **114**, 3804–3808.
72 Y. Cai, H.-K. Mao, P. Chow, J. Tse, Y. Ma, S. Patchkovskii, J. Shu, V. Struzhkin, R. Hemley and H. Ishii, *et al.*, *Phys. Rev. Lett.*, 2005, **94**, 025502.
73 G. Olivieri, A. Goel, A. Kleibert, D. Cvetko and M. A. Brown, *Phys. Chem. Chem. Phys.*, 2016, **18**, 29506–29515.
74 J. Tse, K. Tan and J. Chen, *Chem. Phys. Lett.*, 1990, **174**, 603–608.
75 M. Steele-MacInnis, P. Lecumberri-Sanchez and R. J. Bodnar, *Comput. Geosci.*, 2012, **49**, 334–337.
76 C. D. Cappa, J. D. Smith, K. R. Wilson, B. M. Messer, M. K. Gilles, R. C. Cohen and R. J. Saykally, *J. Phys. Chem. B*, 2005, **109**, 7046–7052.
77 C. D. Cappa, J. D. Smith, B. M. Messer, R. C. Cohen and R. J. Saykally, *J. Phys. Chem. B*, 2006, **110**, 5301–5309.
78 C. N. Rowley and B. Roux, *J. Chem. Theory Comput.*, 2012, **8**, 3526–3535.
79 M. T. H. Nguyen, O. Tichacek, H. Martinez-Seara, P. E. Mason and P. Jungwirth, *J. Phys. Chem. B*, 2021, **125**, 3153–3162.
80 Y. Zeng, Y. Jia, T. Yan and W. Zhuang, *Phys. Chem. Chem. Phys.*, 2021, **23**, 11400–11410.
81 J. Xu, Z. Sun, C. Zhang, M. DelloStritto, D. Lu, M. L. Klein and X. Wu, *Phys. Rev. Mater.*, 2021, **5**, L012801.
82 L. Kong, X. Wu and R. Car, *Phys. Rev. B: Condens. Matter Mater. Phys.*, 2012, **86**, 134203.
83 A. M. Saitta and F. Datchi, *Phys. Rev. E: Stat., Nonlinear, Soft Matter Phys.*, 2003, **67**, 020201.